Maximizing Focus Quality Through Random Media with Discrete-Phase-Sampling Lenses

Qiyuan Wang,[1] Mathias Fink,[2,*] and Guancong Ma[1,†]

[1] *Department of Physics, Hong Kong Baptist University, Kowloon Tong, Hong Kong, China*
[2] *Institut Langevin, ESPCI Paris, Univerité PSL, CNRS, Paris 75005, France*

(Received 15 December 2022; revised 23 February 2023; accepted 23 February 2023; published 27 March 2023)

Wavefronts modulated by a discrete-phase-sampling lens, such as a spatial light modulator or a digital micromirror device, can be brought into focus after propagating through a random medium. Such techniques are a cornerstone for wave manipulations in multiple scattering environments. In this work, we examine prevailing focusing protocols, including matched filtering and inverse filtering, from the perspective of focus quality, which is defined as the contrast between the energy delivered to the focal peak and the total transmitted energy. Our results show that conventional protocols have limitations in achieving the best focus quality. Based on these analyses, we present an improved wavefront-shaping protocol that directly prioritizes focus quality. The influence of phase sampling resolutions is also analyzed in conjunction with these focusing protocols. Our results can merit the future design and implementation of intelligent lenses, which may potentially benefit various disciplines such as energy delivery, imaging, and communication.

DOI: 10.1103/PhysRevApplied.19.034084

I. INTRODUCTION

Focusing of waves such as light, microwaves, and sound is one of the foundations of wave-based applications. Focusing is also closely related to imaging techniques. It is widely believed that the generation of a focal spot merely requires the modulation of an impinging wavefront such that the wavefield constructively interferes at a designated point. Such a goal is relatively simple to achieve in free space with a lens made of a homogenous piece of material with curved surfaces. Thanks to the development of various multiple-scattering wave techniques such as time reversal of waves and wavefront/wavefield shaping [1–4] together with the hardware components, i.e., tunable lenses such as time-reversal mirrors [5–7], spatial wave modulators (SWMs) [8–10], and digital micromirror devices, it is now even possible to focus a wave through or inside a disordered, random medium [2,11–13]. Such a breakthrough benefits a wide range of applications, e.g., energy storage and delivery [14–17], wireless communication [18–21], ultrasound sensing and imaging [22–25], reverberation control [10,26,27], and optical computing [28,29].

All these applications can benefit from higher focus quality. The ideal focus means that the wave energy is delivered entirely to the designated location but vanishes elsewhere. In other words, focusing is not only the concentration of waves at a desirable location but also their removal from the background. However, this ideal situation can never happen in ordinary media because any incoming waves must interfere with diverging waves, and the outcome is a diffraction-limited hotspot accompanied by sidelobes. For focusing through a random medium, there is an additional constraint originating from the limitation of spatial sampling, i.e., most of the tunable lenses applied can only modulate the phase or amplitude of a wavefront in discretized steps. Therefore, the rasterized phase and amplitude profiles inevitably deviate from the ideal, smooth profile, which generates an unfocused wavefield that contaminates the background and, hence, lowers the focus quality. Despite the extensive research in focusing through random media, so far there have been few studies on the focus quality generated through a random medium.

In this work, we investigate how the discrete-phase-sampling (DPS) process of tunable lenses affects the focus quality. A numerical model is developed to simulate the focusing process with DPS lenses (DPSLs) through random media in a two-dimensional (2D) configuration. We first study focusing in free space as an example, then dive into the problem of focusing through random media. Prevailing focusing protocols, including matched filtering (MF, which in our case corresponds to both wavefront shaping and phase conjugation) and inverse filtering (IF), are studied comprehensively and compared at

*mathias.fink@espci.fr
†phgcma@hkbu.edu.hk

different phase sampling resolutions. In addition, an alternative technique called contrast-based wavefront shaping (CWFS) is proposed for achieving the highest focus quality. Our study is based on a 2D scalar-wave model, making it directly applicable to acoustics and ultrasound, in which one-dimensional (1D) transducer arrays are common. However, the model can in principle be adapted to other types of waves and three-dimensional (3D) configurations upon additional modifications. It also provides benchmarks for the design and evaluation of modern tunable lenses as well as their performances with various multiple-scattering techniques, and suggests a simple yet robust protocol that can go beyond conventional limitations and maximize focus quality.

II. FOCUS QUALITY OF FRESNEL AND DPS LENSES IN FREE SPACE

First, we demonstrate the deterioration of focus quality by DPSLs using a simple example in free space. Our configuration is to use a Fresnel lens with aperture D to generate one focal spot at a distance f with a 2D plane wave, as shown in Fig. 1(a). The working principle of the Fresnel lens is to compensate the phase differences between all positions on the incident wavefront to the focal spot, which is chosen to be $(x,z) = (0,f)$. The phase differences are given by $k\left(\sqrt{f^2+x^2}-f\right)$, where $k = 2\pi/\lambda$ is the wavenumber for the considered wavelength λ. The ideal phase profile for the lens is, thus, $\theta(x) = -k\left(\sqrt{f^2+x^2}-f\right)$, and is plotted as the red line in Fig. 1(b). Numerically, we use the Huygens-Fresnel principle [30,31] to generate the modulated wavefield, i.e., each point at the incident plane ($z = 0$) acts as a secondary point source. The wavefield in the focal plane is then calculated by combining all the wavefields induced by the secondary waves. Because our model is 2D, the point sources emit cylindrical waves described by the Hankel function. Because we observe at the far field, it is replaced by the asymptotic form to simplify the computation [32]. The propagation in free space between the lens and the focal plane is connected by a matrix

$$P_f = \mathbf{F}(f)P_i, \tag{1}$$

where P_i and P_f are $N \times 1$ vectors representing the wavefield vectors at the incident and focal plane, respectively, and $\mathbf{F}(z)$ is a $N \times N$ matrix describing the propagation in free space. Its entries are given by $\mathrm{F}_{mn}(z) = \left(d/\sqrt{i\lambda}\right)\left(e^{ikr_{mn}}/\sqrt{r_{mn}}\right)$, where $r_{mn} = \sqrt{z^2+[(n-m)d]^2}$, $m,n = 1,\ldots,N$, and $d = D/N$ is the spatial pitch between two adjacent points.

The intensity distribution $|\mathcal{P}(x)|^2$ obtained at the focal plane is shown in Fig. 1(c). To evaluate the focus quality $\mathcal{Q}$, which is defined as the ratio between the focused energy and the total energy delivered to the focal plane,

$$\mathcal{Q} = \frac{\int_{x_1}^{x_2}|\mathcal{P}(x)|^2dx}{\int_{-D/2}^{D/2}|\mathcal{P}(x)|^2dx}, \tag{2}$$

where $\mathcal{P}(x)$ is the wave distribution at the focal plane, that is numerically sampled by the vector P_f, and x_1, x_2 are given by the width of the main peak. Here, the system parameters are $\lambda = 0.2$ m, $f = 10$ m, $D = 9.9$ m, and $dx = d = 0.02$ m is the spatial resolution in our numerical calculation. The spatial resolution is fine enough to obtain precise wavefields. The maximum possible value of $\mathcal{Q}$ value is one, which means all wave energy is delivered to a focal peak. Using Eq. (2), the ideal Fresnel lens creates a focus with $\mathcal{Q} \approx 0.87$. This value is due to the fact that, in free space, focal spot formed by waves is always accompanied by sidelobes caused by the interference, and some energy is delivered to the sidelobes instead of the main focal peak.

For DPSLs, however, the focus qualities deteriorate from this optimal value. The black and green lines in Figs. 1(b) and 1(c) plot the phase profiles and corresponding focusing distributions of a 2-phase DPSL, i.e., a binary phase-modulating DPSL, and a 36-phase DPSL, based on the phase profile of the Fresnel lens. The focus quality for the 2-phase DPSL is reduced to $\mathcal{Q} \approx 0.63$. The deterioration is clearly visible in Figs. 1(c) and 1(e): not only are the sidelobes around the focal spot larger, but the background is also contaminated (detailed derivations are demonstrated in Appendix A). The deterioration is clearly due to nonideal phase profile caused by the sparse phase-sampling resolution, denoted p. When p is sufficiently large, e.g., $p = 36$, the background is much cleaner and the focus profile is nearly indistinguishable from the ideal Fresnel lens, as shown in Figs. 1(c) and 1(f). In Fig. 1(d), the focus quality $\mathcal{Q}$ is plotted as a function of p. It is seen that $\mathcal{Q}$ first increases with p then saturates around $p = 8$.

III. FOCUS QUALITY OF DPS LENSES THROUGH RANDOM MEDIA

Next, we continue to use the 2D numerical model to investigate the focus quality by DPSLs through random media. To focus through random media, multiple-scattering techniques and DPSLs are necessary. The configuration is similar to that of the free space, and it is shown schematically in Fig. 2(a). The multiple-scattering region (gray) is placed between the DPSL (green) and a region of free space (blue). The propagation of an impinging plane wave goes through three steps: first, it receives the phase modulation by the DPSL; second, the modulated wave enters the random medium and experiences multiple scattering; third, the wave that exits from the random medium (the exit plane is defined as $z = 0$) propagates through a distance in free space, then creates a hot spot at the targeted

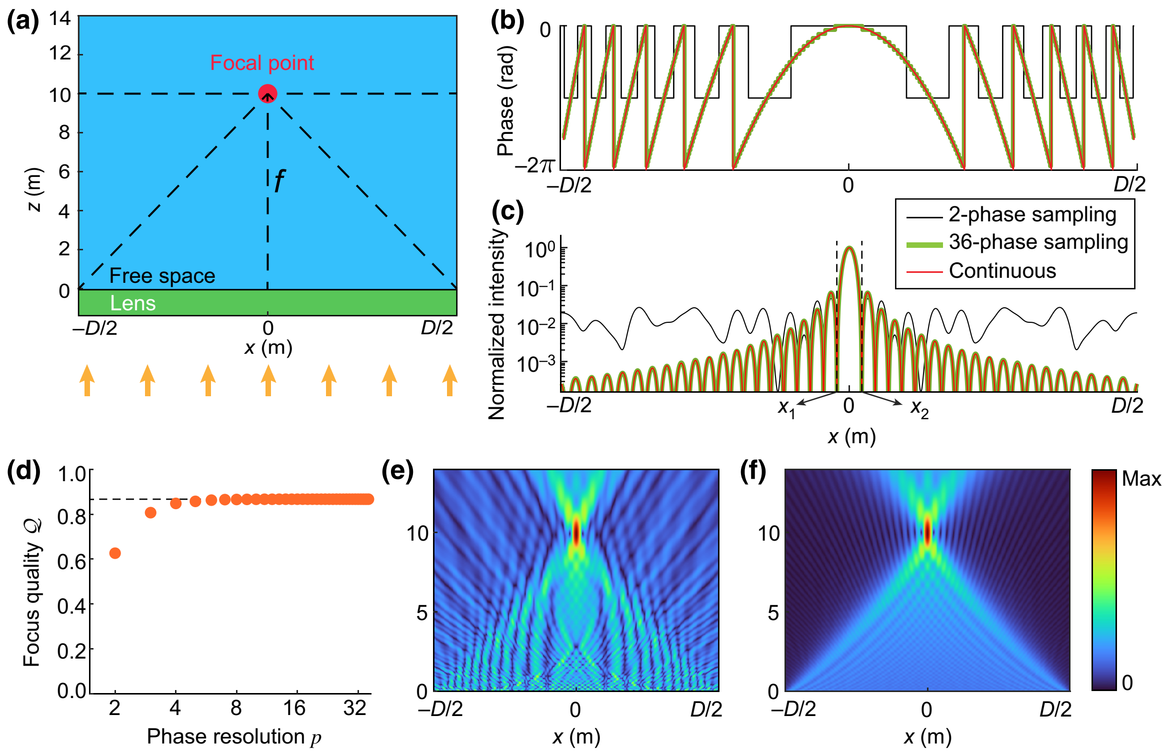

FIG. 1. Focusing with a Fresnel lens in free space. (a) Schematic of the configuration. The blue and green regions represent free space and lens, respectively, and the red circle marks the focal spot. A plane wave (yellow arrows) impinging upon the lens receives phase modulations and creates a focus at the focal spot. (b) The phase profiles of an ideal Fresnel lens (red) and DPSLs with phase resolutions $p = 2$ (black) and $p = 36$ (green). (c) The normalized one-dimensional (1D) intensity distributions $|\mathcal{P}(x)|^2$ at the focal plane by ideal and DPS Fresnel lenses with different p. (d) Focus quality $\mathcal{Q}$ achieved with different p. The x axis is in a logarithmic scale with base 2. (e) The normalized two-dimensional (2D) amplitude field of a 2-phase DPSL. (f) The normalized 2D amplitude field of a 36-phase DPSL. The focal length is chosen as $f = 10$ m, and the aperture width is $D = 9.9$ m.

focal spot $(0, f)$. This process is represented by

$$P_f = \mathbf{F}(f)\mathbf{K}P_i = \mathbf{H}P_i, \tag{3}$$

where $\mathbf{F}(f)$ is the matrix representing the propagation in the free space, $\mathbf{K}$ is the transmission matrix for the random medium, which is modeled using a random matrix [11], $\mathbf{H} = \mathbf{F}(f)\mathbf{K}$ is the net propagator for the problem (the numerical details are described in Appendix B). The physical parameters are the same as the free space model: $\lambda = 0.2$ m, $f = 10$ m, and $D = 9.9$ m. We do not consider the thickness of the random medium as well as the lens because, for our configuration, the diffraction properties of a focusing are determined by the propagation distance after the random medium and its aperture [33]. To avoid correlations among DPSL pixels in lateral dimension, the spatial pitch between adjacent pixels is chosen to be half the wavelength, i.e., $d = \lambda/2 = 0.1$ m [14,34], then the dimension of the matrices and vectors is $N = D/d = 99$. The degrees of freedom of the modulation, i.e., the number of controllable pixels in a lens is therefore the same as the matrix's dimension N. The $\mathbf{K}$ matrices are generated such that the singular value distributions follow the quarter-circle law, indicating no correlation among matrix elements. This is achieved by downsampling a 990×990 full transmission matrix to 99×99 [35] which shifts from bimodal eigenvalue statistics (of $\mathbf{K}^\dagger\mathbf{K}$) [11,36] to quarter-circle singular value statistics (of $\mathbf{K}$) [8,37]. Physically, this setting describes focusing scenarios wherein only a small part of the information is accessible due to the limited aperture, such as focusing through a slab of white paint or biological tissues. Thus, the pixels on the DPSL independently control different sets of scattering channels, and the controlled channels are uncorrelated with each other. (Focusing through random media with bimodal transmission distributions is also investigated, and similar results are obtained. See Appendix C.)

A. Matched filtering and inverse filtering

The focal spot is generated using three different protocols. The first is the MF that only maximizes the local field at the focal spot [1]. The second is the IF that manages to focus by constructing an inverse propagator to retrieve the optimal focus pattern [38]. The third is called contrast-based wavefront shaping (CWFS). It

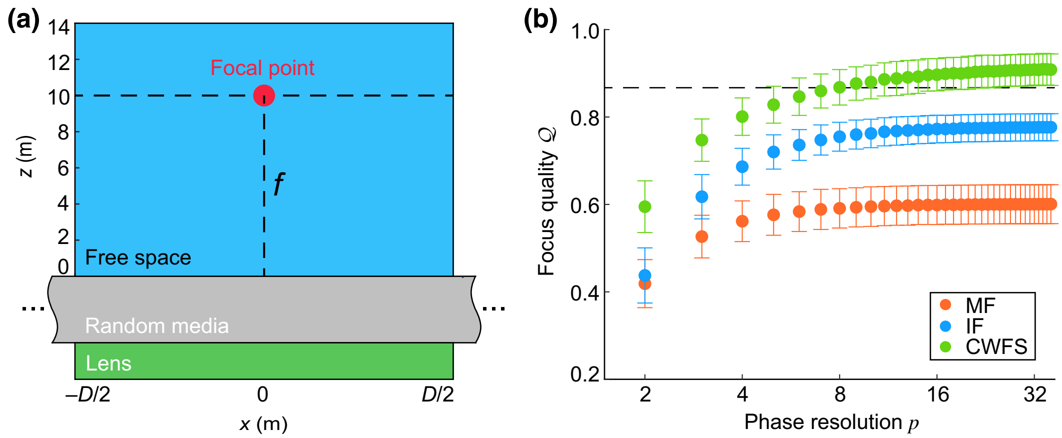

FIG. 2. Focusing through random media. (a) Schematic drawing of the configuration. The blue, gray, and green regions represent free space, random medium, and the DPSL, respectively. (b) Focus quality $\mathcal{Q}$ as functions of phase resolution p for different focusing protocols. Orange, blue, and green circles represent matched filtering (MF), inverse filtering (IF), and contrast-based wavefront shaping (CWFS), respectively. The number of iterations for CWFS here is 10. The dashed black line indicates the focus quality achieved by the Fresnel lens in free space ($\mathcal{Q} \approx 0.87$). The results are averaged over 1000 realizations, and the standard deviations in the data are indicated by the error bars. The focal length is chosen as $f = 10$ m, and the aperture is $D = 9.9$ m.

is a protocol modified from the conventional wavefront shaping (WFS), which has an adjusted optimization goal to favor better focus quality. The average focus qualities of these three protocols are obtained with different phase sampling resolutions p, as plotted in Fig. 2(b). For all protocols, the focus qualities increase with p until they plateau. Figure 2(b) also suggests that, for practical purposes, $p = 8$ or 10 would already be quite sufficient because the performance gained by having even higher p is minuscule.

Next, we analyze the performances of these protocols. MF can be achieved by two seemingly distinctive approaches. The first is conventional WFS [3], an iterative optimization process that requires the measured local field at the focal spot as feedback for the DPSL to achieve a desirable phase modulation. The second is phase conjugation (PC) [34], which is based on spatial reciprocity. The first step of PC is to treat the focal spot as a source that sends a wave which is measured at the lens plane. This propagation is described by the matrix $\mathbf{Q}_{\mathrm{PC}} = \mathbf{K}^{\mathrm{T}}\mathbf{F}^{\mathrm{T}}$, which is the backward propagator. In the second step, the measured field is phase-conjugated and sent back from the incident plane. Because our DPSL only modulates phases, only the phase profile is taken, which reads $P_i = e^{i\phi_{\mathrm{PC}}}$ and

$$\phi_{\mathrm{PC}} = \arg(\mathbf{Q}^{*}_{\mathbf{PC}}\Delta), \tag{4}$$

where $\Delta = (0, \ldots, 1, \ldots, 0)^{\mathrm{T}}$ represents the initial wave sent at the focal spot. For a DPSL, ϕ_{PC} is further sampled to the nearest available phase at all pixels. Despite the procedural differences between WFS and PC, they both equivalently generate a spatial matched filter for the incident wave, hence they achieve the same outcome, as plotted in Figs. 2(b) and 3(a). Because MF only concerns the amplitude at the focal spot but not the entire field in the focal plane, it is not optimal when the focus quality $\mathcal{Q}$ is an important criterion.

The second protocol is the IF, and it achieves better focus quality. The process of IF is similar to PC. The focal spot described by Δ is also treated as a source, and the backward propagator to the lens plane is $\mathbf{Q}_{\mathrm{IF}}$. Unlike PC, IF constructs an inverse propagator by pseudoinversion based on singular value decomposition. In short, the propagator $\mathbf{H}$ is decomposed as $\mathbf{H} = \mathbf{U}\Sigma\mathbf{V}^{\dagger}$, where $\mathbf{U}$ and $\mathbf{V}$ are $N \times N$ unitary matrices containing the singular vectors of the propagator († denotes conjugate transpose), and Σ is a rank-deficient diagonal matrix whose nonzero elements σ_n are the singular values. The inverse propagator is then numerically constructed by inversing all the effective singular values (i.e., σ_n are reversed to σ_n^{-1} and form the matrix $\hat{\Sigma}^{-1}$) and reads $\mathbf{Q}_{\mathrm{IF}} = \mathbf{V}\hat{\Sigma}^{-1}\mathbf{U}^{\dagger}$ (the readers can refer to Refs. [1,38] for details of the process). Tikhonov regularization is used to mitigate the numerical noise caused by the small singular values so that the inversion process is numerically stable [34]. In short, $\mathbf{Q}_{\mathrm{IF}}$ is replaced by a mean-square optimized operator $\bar{\mathbf{Q}}_{\mathrm{IF}} = (\mathbf{H}^{\dagger}\mathbf{H} + \mu\mathbf{I}_N)^{-1}\mathbf{H}^{\dagger}$, where μ is the variance of all the redundant elements in $\mathbf{U}$ and $\mathbf{V}$ with small singular values that do not contain information (i.e., the elements within all singular vectors that correspond to a sufficiently small singular value). The modulation is then obtained as $\bar{\mathbf{Q}}_{\mathrm{IF}}\Delta$. Although, in principle, both the amplitude and phase modulations are required for performing IF, we find that taking only the phase information of $\bar{\mathbf{Q}}_{\mathrm{IF}}\Delta$ can also achieve focusing with a contrast higher than the MF. Here, the required modulation of a phase-modulating lens is given

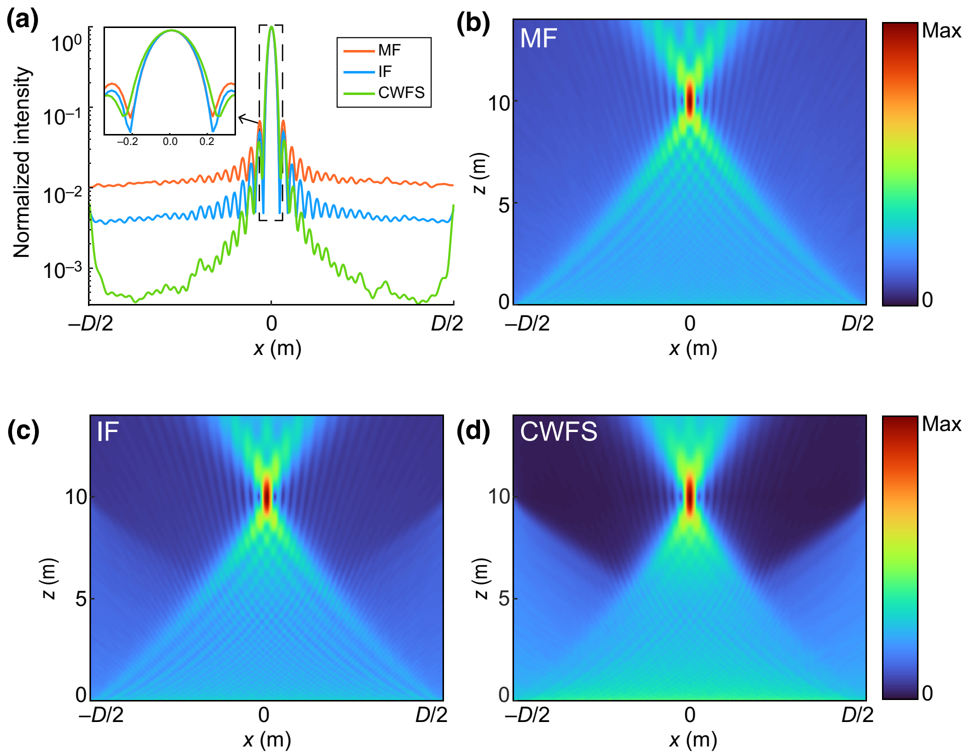

FIG. 3. Focusing through random media with different protocols. (a) The normalized 1D intensity distributions at the focal plane with MF (orange), IF (blue), and CWFS (green). (b)–(d) The normalized 2D amplitude fields of focusing with (b) MF, (c) IF, and (d) CWFS. The number of iterations for CWFS here is 10. The results are produced by 36-phase DPSLs averaged over 1000 numerical realizations.

by $P_i = e^{i\phi_{\rm IF}}$, and

$$\phi_{\rm IF} = \arg(\bar{\mathbf{Q}}_{\rm IF}\Delta) = \arg[(\mathbf{H}^\dagger\mathbf{H} + \mu\mathbf{I}_N)^{-1}\mathbf{H}^\dagger\Delta]. \quad (5)$$

Similar to PC, P_i is further sampled to the nearest available phase when passing through the DPSL. The outcome of IF is consequently calculated by Eq. (3), and the result is shown in Fig. 3(a). Therein, it is clearly seen that the improved focus quality over MF is due to the suppression of background, i.e., waves away from the focal spot. We note that an ideal IF also modifies the amplitudes of the incident wavefront. The results are shown and discussed in Appendix D.

However, IF is still not optimal for focus quality. This may sound surprising because if Δ is ideally reconstructed in the focal plane, then we should automatically have $\mathcal{Q} = 1$, which is the upper limit for $\mathcal{Q}$. However, in reality, the focal spot is always diffraction limited. As a result, IF also needs to take care of minimizing peak width, and the price is a lower contrast [38].

B. Contrast-based wavefront shaping

Here, we present an alternative method called CWFS. As its name suggests, CWFS is based on the WFS, but it has a different optimization objective. Instead of maximizing the amplitude at the focal spot, the algorithm directly maximizes the contrast between the focal spot and the average background, which is given by

$$q = \frac{|\mathcal{P}(0)|}{(1/D)\int_{-D/2}^{D/2}|\mathcal{P}(x)|\mathrm{d}x}, \quad (6)$$

where $\mathcal{P}(x)$ is the wave distribution at the focal plane. Equation (6) is slightly different from the definition of $\mathcal{Q}$. This is because, prior to and during the optimization, the protocol targeting $\mathcal{Q}$ does not know where the maximal of the peak is, and it may generate a distorted focus to maximize $\mathcal{Q}$. Nevertheless, the CWFS produces the best $\mathcal{Q}$ among all three protocols for all phase-sampling resolutions, as shown in Fig. 2(b). The wavefields shown in Fig. 3 further confirm this result, wherein CWFS clearly gives the best result in terms of focus quality: a sharp peak at the focal spot with the cleanest background. The CWFS is superior even at the scarcest phase sampling resolution ($p = 2$), as shown in Fig. 4. In this case, the average focus quality $\mathcal{Q} \approx 0.59$, which is close to that achieved in free space at same phase resolution ($\mathcal{Q} \approx 0.63$). It can even exceed the free space $\mathcal{Q}$ when $p \geq 8$, which implies that with proper technique, the multiple scatterings of

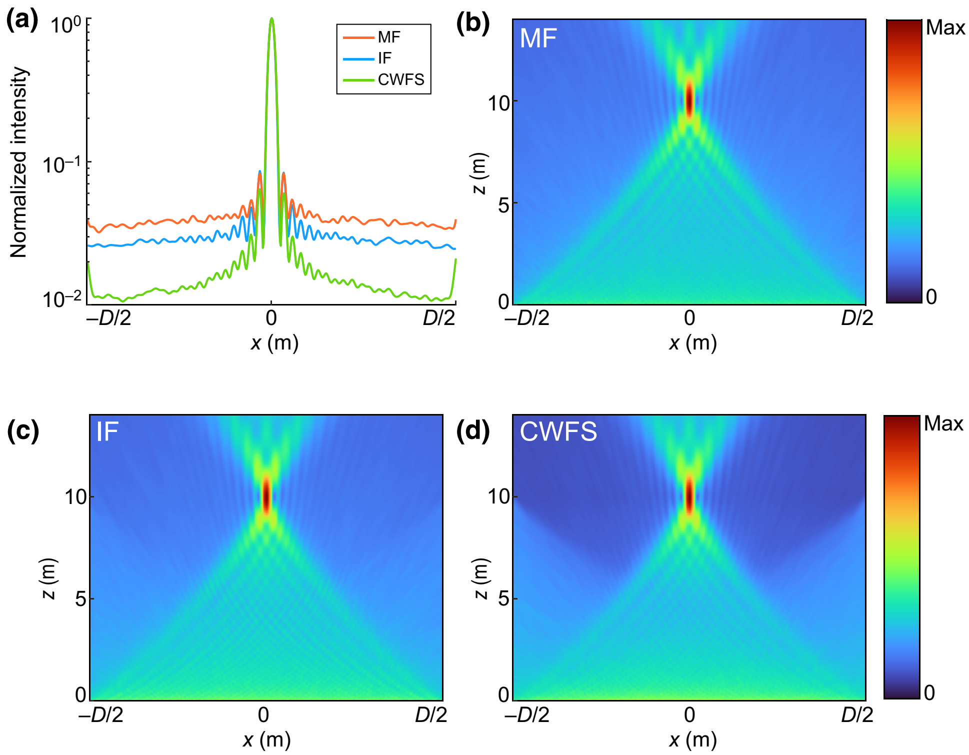

FIG. 4. Focusing through random media with different protocols using 2-phase DPSLs. (a) The normalized 1D intensity distributions at the focal plane produced with MF (orange), IF (blue), and CWFS (green). (b)–(d) The normalized 2D amplitude fields of focusing with (b) MF, (c) IF, and (d) CWFS. The number of iterations for CWFS here is 10. The results are averaged over 1000 numerical realizations.

the random media can indeed benefit rather than hinder high-quality focusing.

It is also observed in Fig. 2(b) that the performance of CWFS saturates slower, suggesting that it benefits more from a higher p counts compared with the other protocols. This is because CWFS needs to correlate the focus spot with the background, thus it demands more detailed control over the shaped wavefront. Hence CWFS can benefit much more from the ability to access more degrees of freedom enabled by a higher p. This is implied in Eq. (6). The CWFS essentially requires information on the entire wavefield in the focal plane. The performance of the CWFS

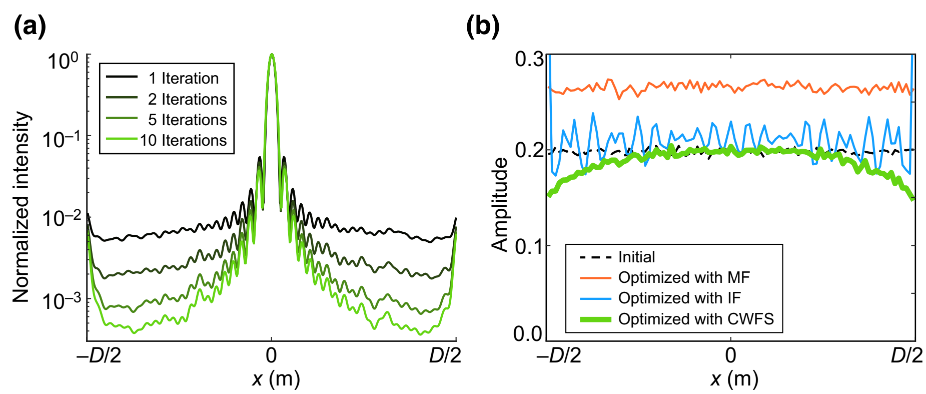

FIG. 5. Characteristics of the CWFS. (a) The normalized 1D intensity distributions at the focal plane. More iteration rounds are desirable because CWFS induces correlations between pixels. The performance saturates around 10 rounds of iterations. (b) The average amplitude distributions at the exit plane of the random media ($z = 0$). The solid lines are the results optimized with MF (orange), IF (blue), and CWFS (green), respectively. The black dashed line plots the initial level before any optimization. The amplitude distribution of CWFS is tapered near the edges, indicating an aperture apodization effect. The number of iterations for CWFS here is 10. All the results are calculated using 36-phase DPSL and averaged over 1000 realizations.

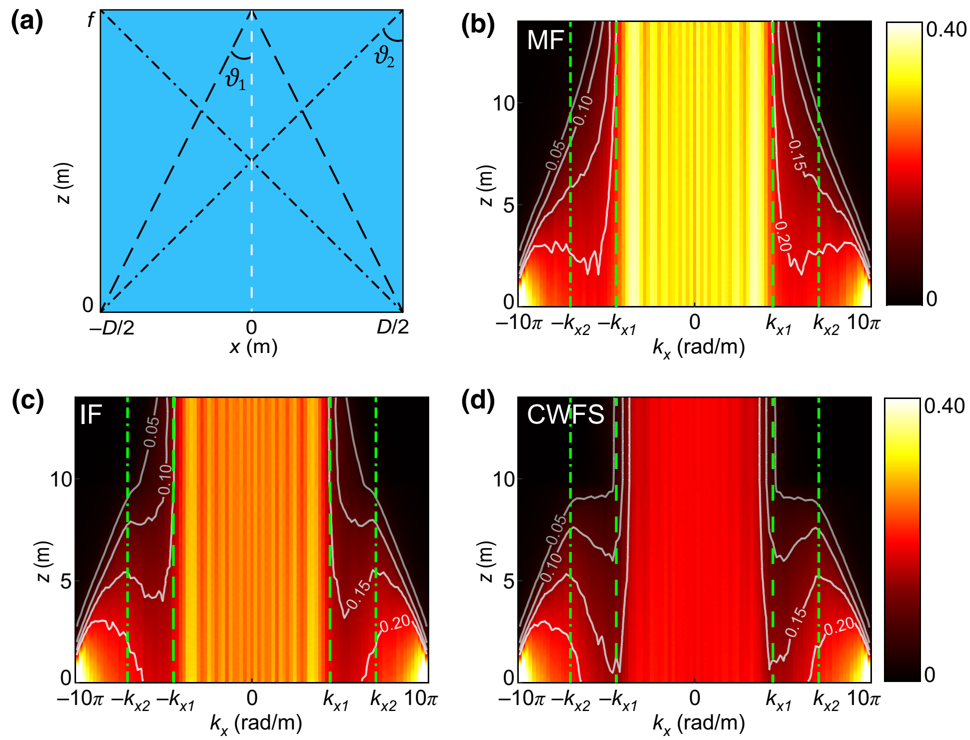

FIG. 6. The normalized k_xz fields of the focusing wavefields shown in Fig. 3. (a) Graphical explanation of the angles ϑ_1 (dashed lines) and ϑ_2 (dashed-dotted lines). (b)–(d) k_xz fields with (b) MF, (c) IF, and (d) CWFS. The number of iterations for CWFS here is 10. The contours in (b)–(d) indicate the magnitudes of k_x components.

thus also benefits from higher iteration times. This point can be understood from Eq. (3). Although with similar algorithms, only one iteration time is sufficient for WFS to achieve the optimal outcome because it only measures and optimizes the focal spot. (Here, one iteration refers to examining all DPSL pixels for one round.) In other words, it involves only one row of the propagator matrix **H**, with each element independently relating to only one entry in P_i, so that there are no correlations among the optimal phase of each pixel. In contrast, CWFS optimizes the entire wavefield vector, therefore, it engages the entire propagator. It follows that the optimal state of a particular pixel is dependent on the states of other pixels. In an iterative optimization scheme, this effect indicates that the outcome can benefit from more rounds of optimizations, as shown in Fig. 5(a), wherein the performance of CWFS increases with iteration times and saturates around 10 rounds.

A closer look at the wavefield generated with CWFS [Figs. 3(a), 3(d), 4(a), and 4(d)] reveals some intriguing aspects. First, the sidelobes are suppressed compared to both MF and IF. This is related to the observation in Fig. 5(b), that is, the wavefield exiting from the random media, i.e., at $z = 0$, has a distinctive distribution along the x direction. Therein, the wavefield optimized with CWFS is weaker in amplitude near the boundaries at $x = \pm(D/2)$. It then becomes that the CWFS drives the DPSL to equivalently impose aperture apodization through random media, which is an effective technique in reducing sidelobes [39]. Closer examination shows that the focal peak generated by CWFS is slightly increased in width [inset of Fig. 3(a)], which is also consistent with the conventional outcome of aperture apodization. In other words, the random media are utilized to establish amplitude modulation even the DPSL only modulates phases. We remark aperture apodization on the incident wave before the random media generates no observable effect on the focus because such amplitude modulations are scrambled by the multiple scatterings. However, here, the "apodization" introduced by CWFS is the net outcome from both the DPSL and the random media. This also qualitatively explains why the CWFS can surpass the performances of the others.

Second, in addition to the focusing wavefront, the CWFS appears to generate a diverging wavefront, such that the waves appear to be "steered away" for a clean background in the focal plane. This characteristic is also seen for the IF wavefield, which implies a connection between the two protocols [Figs. 3(c), 3(d), 4(c), and 4(d)]. To analyze this effect, we perform spatial Fourier transform on the focusing wavefields [Figs. 3(b)–3(d)] for the x direction. The results are plotted in Figs. 6(b)–6(d), where $k_x = 2\pi \sin\vartheta/\lambda$ with ϑ being the angle between the wavevector and z axis [see Fig. 6(a)]. For the converging wavefront that contributes to the focus at $(0, f)$, this angle is between 0 and $\vartheta_1 = \tan^{-1}(D/2f)$,

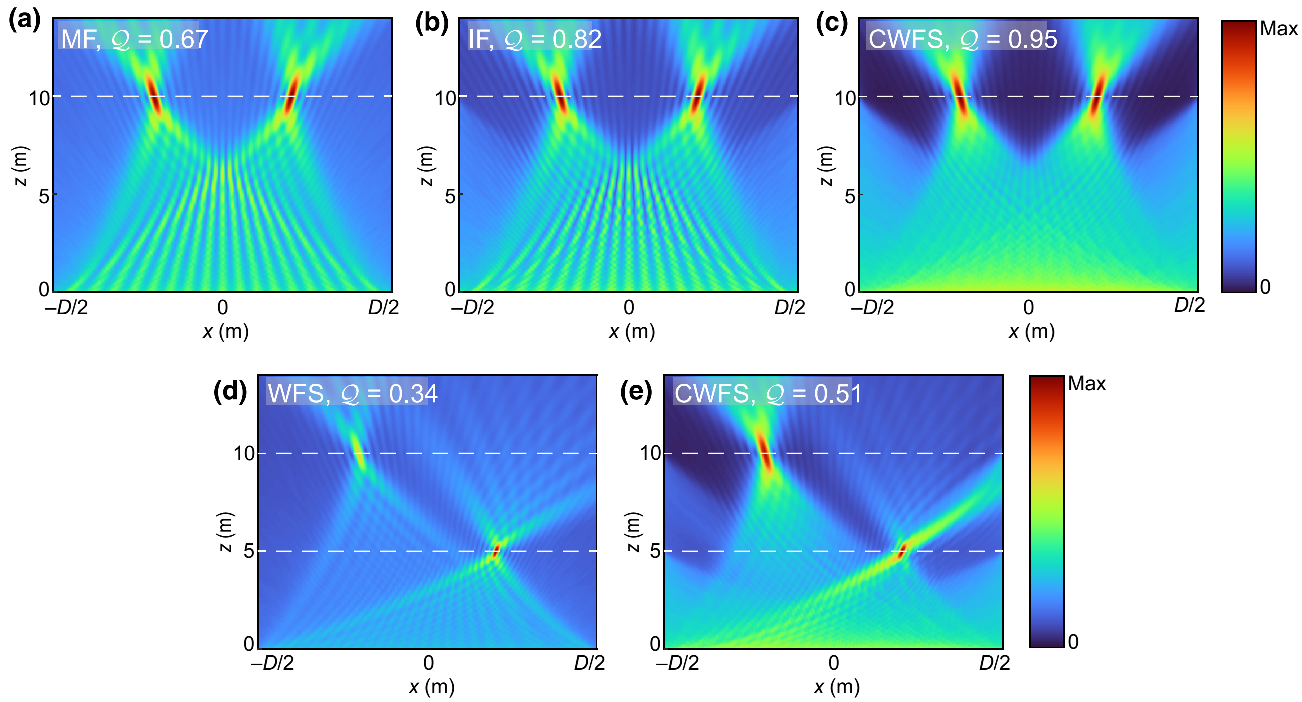

FIG. 7. (a)–(c) Two-point focusing at the same focal plane. The normalized 2D amplitude fields optimized with (a) MF, (b) IF, and (c) CWFS. (d),(e) Two-point focusing at different focal planes. The normalized 2D amplitude fields optimized with (d) WFS and (e) CWFS. The number of iterations for CWFS here is 10. The focal points are chosen at $x_\alpha = -2$ m, $f_\alpha = 5$ m and $x_\beta = 2$ m, $f_\beta = 10$ m. The phase resolution is $p = 36$. The results are averaged over 1000 numerical realizations.

which gives $k_{x1} = 4.44\pi$. This is verified in Figs. 6(b)–6(d), wherein the majority of k_x components fall within this range for all protocols. On the other hand, the diverging wavefront must owe to waves with $|k_x| \geq k_{x2} = 2\pi \sin\vartheta_2/\lambda = 7.04\pi$ where $\vartheta_2 = \tan^{-1}(D/f)$, such that they do not reach the focal plane. Such components are seen for all three protocols in Figs. 6(b)–6(d), but they are clearly more prominent for IF and CWFS, as highlighted by the contours. Meanwhile, for $z > f$, it is seen that k_x components larger than k_{x1} are suppressed for both IF and CWFS, showing that the diverging waves indeed do not reach the focal plane. The suppression is particularly obvious for CWFS, which manifests as a sharp drop at the focal plane $z = f$. This agrees with the fact that the criterion of CWFS [Eq. (6)] explicitly demands background suppression at the focal plane. Interestingly, the diverging wavefronts produced by IF and CWFS can maintain their spatial profiles while propagating in the free space: they exhibit characteristics of nondiffractive beams, such as Bessel beams [40,41], Airy beams [42], and other types of self-bending beams [43,44].

C. Quality of more complex focusing patterns

Here we investigate more complex scenarios. First, we consider the generation of two focal spots at the same focal plane. For PC and IF, this effect is achieved by simply redefining $\Delta = (0,\ldots,1,\ldots,1,\ldots,0)^{\mathrm{T}}$, i.e., by introducing a second virtual source. For WFS, it requires an additional probe at the second focal spot, and the optimization is modified to target the total field amplitude measured by the two probes. For CWFS, $q_,$ [Eq. (6)] is also modified to include the contribution of the second focal spot. In Figs. 7(a)–7(c), we show the results with the two focal spots at $x_\alpha = -2$ m, $x_\beta = 2$ m, and $f = 10$ m. CWFS clearly gives the highest quality.

WFS and CWFS can also be easily modified to simultaneously generate focal spots at different focal planes. (Of course, it is also possible for PC and IF to achieve a similar result, but the virtual sources take far more complicated forms so they are far less convenient compared with WFS and CWFS.) An example is shown in Figs. 7(d) and 7(e), where the two focal spots are set at $x_\alpha = 2$ m, $f_\alpha = 5$ m and $x_\beta = -2$ m, $f_\beta = 10$ m. CWFS clearly achieves higher focus quality, and the background suppression is clearly seen as the incident wavefront of the first focal spot is highly "skewed" such that the contamination to the background at the second focal plane ($f_\beta = 10$ m) is minimized. These results demonstrate the reliability and robustness of the CWFS protocol for producing complex focusing.

IV. DISCUSSION AND CONCLUSION

The focusing scenarios studied here are based on an extension of the Fresnel lens, which involves only one wavelength. A Fresnel lens is a monochromatic device because the phase profiles for waves with different wavelengths must be different. However, focusing through random media is intrinsically broadband because the multiple scatterings effectively scramble the Fresnel zones for different wavelengths, such that a DPSL can access them simultaneously. Therefore, we expect the CWFS to be equally effective in broadband focusing. Studies on time-reversal focusing [6,45–47] and multispectral transmission matrices [48] may be useful in guiding the implementation.

Although our study is based on 2D configurations, the numerical model that is based on the Huygens-Fresnel principle can be straightforwardly modified for studying 3D configurations by changing the cylindrical monopole sources to spherical versions. In that case, an even higher-contrast focus is expected because the amplitude of spherical wave declines faster in 3D space compared with cylindrical wave in 2D space, resulting in a smaller background level. However, much greater computational power is needed to handle the drastically increased data size that comes with the additional dimensionality. In addition, polarization can also be considered, which requires the degree of freedom of the system to be doubled, i.e., involving two orthogonal polarization components [49,50].

To conclude, we have studied the focusing by DPSLs through random media in a 2D configuration from the perspective of focus quality. Three prevailing focusing protocols are analyzed together with the effect of phase sampling resolution. We then propose and analyze a different protocol called CWFS which prioritizes high contrast between the focal spot and background at the focal plane. Our results can be useful in the design and evaluation of intelligent lenses, which potentially benefit the field of ultrasound imaging and a wide range of other wave and light-based applications such as beamforming, energy harvesting, source localization, communication, optical, or acoustic force applications.

ACKNOWLEDGMENTS

G.M. thanks Sébastien Popoff for fruitful discussions. This work is supported by the National Natural Science Foundation of China (11922416) and the Hong Kong Research Grants Council (RFS2223-2S01, 12302420, 12300419, 12301822). M.F. acknowledges partial support from the Simons Foundation/Collaboration on Symmetry-Driven Extreme Wave Phenomena.

APPENDIX A: DPS FRESNEL LENS IN FREE SPACE

The phase profile of a Fresnel lens is discretized into p steps, i.e.,

$$\varphi_n = \frac{2(n-1)\pi}{p}, \tag{A1}$$

with $n = 1, 2, \ldots, p$. To achieve focusing, these finite phases need to be matched to the optimal phase profile $\theta(x) = -k\left(\sqrt{f^2 + x^2} - f\right)$ with the nearest true value. The optimal matching profile given by this process can be written as a step function with variable θ:

$$\varphi(\theta) = \sum_{n=1}^{p} \varphi_n \chi_{\Theta_n}(\theta), \tag{A2}$$

where

$$\chi_{\Theta_n}(\theta) = \begin{cases} 1, & \text{if} \theta \in \Theta_n, \\ 0, & \text{if} \theta \notin \Theta_n, \end{cases} \tag{A3}$$

and

$$\Theta_n = \left(\frac{2n-3}{p}\pi, \frac{2n-1}{p}\pi\right]$$

We then express the modulation of the lens $e^{i\varphi(\theta)}$ as Fourier series

$$\begin{aligned} e^{i\varphi(\theta)} &= \varepsilon(p) \sum_{l=0}^{\infty} \left[\frac{(-1)^l}{pl+1} e^{i(pl+1)\theta} + \frac{(-1)^l}{pl+p-1} e^{-i(pl+p-1)\theta}\right] \\ &= \varepsilon(p)\left[e^{i\theta} + \frac{1}{p-1} e^{-i(p-1)\theta} + \ldots\right], \end{aligned} \tag{A4}$$

where $\varepsilon(p)$ is the normalization factor. Equation (A4) shows that any DPSL can be equivalently decomposed into a series of lenses, each with a different wave modulation function. The first term represents the original converging lens that perfectly compensates for the phase difference, other terms generate undesirable parasitic waves that are not focusing on the target position. For example, the second term in Eq. (A4) generates a diverging wave with a virtual source located at $[0, -(p-1)f]$ and a relative amplitude of $1/(p-1)$. For the subsequent terms, their relative amplitudes are even smaller. These parasitic waves will interfere with the converging wave in the focal plane, and deteriorate the focus quality. For larger p values, the diverging waves have less impact on the focusing, thus, the focus quality $\mathcal{Q}$ accordingly improves. When the diverging waves are sufficiently small, their influences on $\mathcal{Q}$ are negligible such that $\mathcal{Q}$ reaches to a plateau.

APPENDIX B: NUMERICAL METHODS

Our model involves two propagation regions such that numerically the propagator **H** [Eq. (3)] is the product of two matrices: the free space propagation matrix **F** which is introduced in Eq. (1), and the random transmission matrix

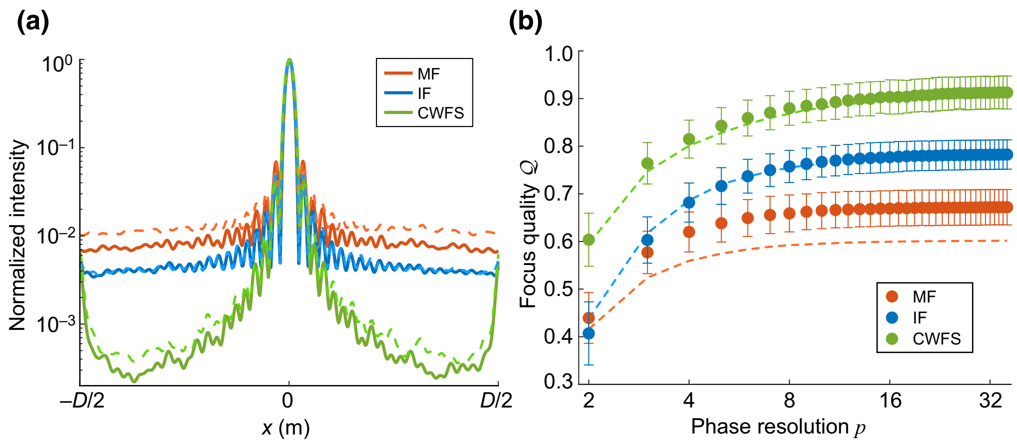

FIG. 8. Focusing through random media with bimodal transmission statistics. (a) The normalized 1D intensity distributions at the focal plane (solid curves). The phase resolution is $p = 36$. For comparison, the dashed curves plot the results in the main text with quarter-circle law statistics [same as in Fig. 3(a)]. (b) Focus quality $\mathcal{Q}$ at different phase resolutions (markers). The dashed curves plot the performances obtained through media obeying quarter-circle statistics [Fig. 2(b)]. The results of CWFS are iterated 10 times. The results are averaged over 1000 realizations, and the standard deviations in the data are indicated by the error bars.

$\mathbf{K}$ which is downsampled from an $\tilde{N} \times \tilde{N}$ full transmission matrix $\tilde{\mathbf{K}}$. $\tilde{\mathbf{K}}$ is taken from one quadratic block of the $2\tilde{N} \times 2\tilde{N}$ scattering matrix $\mathbf{S}$, which is numerically generated as a random unitary matrix [11]. Then, to downsample $\tilde{\mathbf{K}}$ to $N \times N$ dimension, a matrix transformation is applied which reads $\mathbf{K} = \mathbf{A}_2\tilde{\mathbf{K}}\mathbf{A}_1$, where $\mathbf{A}_2(\mathbf{A}_1)$ is an $N \times \tilde{N}(\tilde{N} \times N)$ matrix which is generated by randomly eliminating $\tilde{N} - N$ rows(columns) of an $\tilde{N} \times \tilde{N}$ identity matrix [35].

The outgoing wavefield $\mathbf{K}P_i$ then becomes the incident wavefront at the exit plane $z = 0$ in free space. The incident wavefronts are numerically generated using the Huygens-Fresnel principle. The exit plane with an aperture of $D = 9.9$ m is discretized into $5N$ equally spaced segments, where $N = 99$ is the number of tunable pixels in the DPSL. A point source emitting a cylindrical wave is placed at the center point of each segment. It is then straightforward to work out that the spacing of the point sources is $\lambda/10$, with $\lambda = 0.2$ m. The DPSL effectively modulates five point sources together, such that by neglecting minor deviations between sources, the wavefields at the exit plane $\mathbf{K}P_i$ is reduced to a 99×1 vector. Therefore, the propagator matrix is 99×99 in size.

APPENDIX C: FOCUSING THROUGH RANDOM MEDIA WITH BIMODAL TRANSMISSION STATISTICS

Here, we reexamine the three focusing protocols described in this paper using random matrices following bimodal distribution. In the main text, the random media is modeled by random matrices $\mathbf{K}$ with singular value statistics (the normalized singular value density distribution of $\mathbf{K}$) following the quarter-circle law. Mathematically, this means all the elements within $\mathbf{K}$ are independent of each other, and it is achieved by downsampling a full transmission matrix $\tilde{\mathbf{K}}$ whose eigenvalue statistics (the eigenvalue density distribution of $\tilde{\mathbf{K}}^\dagger\tilde{\mathbf{K}}$) originally follow a bimodal distribution [35]. Physically, such a condition indicates the lens only has limited access to the medium, which is typical for wave/light propagation through multiple scattering media such as a slab of white paint or biological tissues.

However, random media following bimodal distribution do exist, e.g., in a waveguide with disordered scattering inclusions [35,36]. This condition indicates that the multiple-scattering medium will be at the same width as the DPSL aperture. Under such a condition, the lens can access the degrees of freedom of the medium without information loss. (Here, we consider the symmetric bimodal distribution that occurs for chaotic scattering [11], which is a universal condition that does not contain any system-specific information. We note that bimodal distributions can also be asymmetric under diffusive scattering. Such cases are dependent on system details such as mean free path and medium size. They are not considered here.) The results achieved with the three protocols are shown in Fig. 8. The results are largely consistent with those obtained with $\mathbf{K}$ following the quarter-circle law [Figs. 2(b) and 3(a)]. Meanwhile, the results obtained using MF are markedly improved in the bimodal case. This effect originates from the different statistics of $\mathbf{K}$, as the bimodal statistics indicate that the elements within $\mathbf{K}$ are no longer independent but correlated [35,37]. How such interelement correlations affect the performance of MF can be understood from its optimization objective: it only concerns the amplitude at focal spot and does not pay attention to the rest of the wavefield. Then, the wavefield around the focal peak is naturally comprised of the inherent background

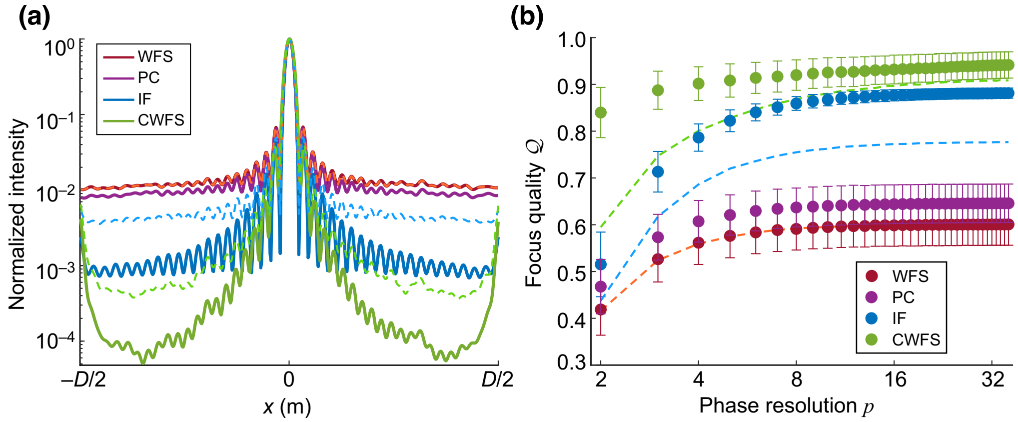

FIG. 9. Focusing through random media with full modulation (discrete phase and amplitude modulation). The amplitude modulations are sampled from 0 to 1 with a step of 0.1. (a) The normalized 1D intensity distributions at the focal plane (solid curves). The phase resolution is $p = 36$. The dashed curves plot the results of phase-only modulations [same as in Fig. 3(a)]. (b) Focus quality $\mathcal{Q}$ with different phase resolution p (markers). The dashed curves plot the performances of phase-only modulations [Fig. 2(b)]. The number of iterations for CWFS here is 10. All results are averaged over 1000 realizations, and the standard deviations in the data are indicated by the error bars.

noises whose level is based on the degree of disorder within the transmission system (described by the propagator $\mathbf{H} = \mathbf{FK}$). Therefore, the more correlations within $\mathbf{K}$, the less disordered the system, and consequently the background level reduces which results in a higher focus quality for MF. On the other hand, because IF and CWFS already consider the whole wavefield (which engage the whole propagator), no significant improvements are observed.

APPENDIX D: FOCUSING THROUGH RANDOM MEDIA WITH MODULATIONS TO BOTH PHASES AND AMPLITUDES

All results shown in the main text are obtained using phase modulation alone. However, for methods such as PC and IF, the ideal modulation profiles should also include modulations to the amplitude of the incident wavefront, i.e., $\mathbf{Q}^{*}_{\mathrm{PC}}\Delta$ and $\bar{\mathbf{Q}}_{\mathrm{IF}}\Delta$ from Eqs. (4) and (5). For the CWFS, amplitude modulation can also be included.

The full modulation results are shown in Fig. 9. Here, the amplitude resolution is fixed at step 0.1 and ranges from 0 to 1, which denotes a fully closed and open pixel, respectively. In Fig. 9, it is seen that all protocols except for WFS (whose results are identical to the phase-modulation-only case) benefit from full modulation, and CWFS still achieves the best focus quality at all phase resolutions. In particular, the CWFS can achieve very high focus quality ($\mathcal{Q} \approx 0.84$) even at binary phase resolution. Such an improvement is not seen for the other protocols. This implies CWFS can take advantage of either phase or amplitude modulation to achieve high-quality focusing, which demonstrates its flexibility in realistic application scenes.

In addition, we note that the two approaches of achieving MF, i.e., WFS and PC, now give different outcomes. Adding amplitude modulation can improve the performance of PC, but it has no improvement on the performance of WFS. This is because its objective is to maximize the amplitude at the focal spot, so that the amplitudes at each pixel will be inevitably optimized to maxima once finding the matched phases.

[1] M. Tanter, J.-L. Thomas, and M. Fink, Time reversal and the inverse filter, J. Acoust. Soc. Am. **108**, 223 (2000).
[2] A. P. Mosk, A. Lagendijk, G. Lerosey, and M. Fink, Controlling waves in space and time for imaging and focusing in complex media, Nat. Photonics **6**, 283 (2012).
[3] I. M. Vellekoop, Feedback-based wavefront shaping, Opt. Express **23**, 12189 (2015).
[4] Z. Yu, H. Li, T. Zhong, J.-H. Park, S. Cheng, C. M. Woo, Q. Zhao, J. Yao, Y. Zhou, X. Huang, *et al.*, Wavefront shaping: a versatile tool to conquer multiple scattering in multidisciplinary fields, Innovation **3**, 100292 (2022).
[5] M. Fink, Time reversed acoustics, Phys. Today **50**, 34 (1997).
[6] J. de Rosny and M. Fink, Overcoming the Diffraction Limit in Wave Physics Using a Time-Reversal Mirror and a Novel Acoustic Sink, Phys. Rev. Lett. **89**, 124301 (2002).
[7] G. Ma, X. Fan, F. Ma, J. de Rosny, P. Sheng, and M. Fink, Towards anti-causal Green's function for three-dimensional sub-diffraction focusing, Nat. Phys. **14**, 608 (2018).
[8] S. M. Popoff, G. Lerosey, R. Carminati, M. Fink, A. C. Boccara, and S. Gigan, Measuring the Transmission Matrix in Optics: An Approach to the Study and Control of Light Propagation in Disordered Media, Phys. Rev. Lett. **104**, 100601 (2010).
[9] N. Kaina, M. Dupré, G. Lerosey, and M. Fink, Shaping complex microwave fields in reverberating media with binary tunable metasurfaces, Sci. Rep. **4**, 6693 (2014).

[10] G. Ma, X. Fan, P. Sheng, and M. Fink, Shaping reverberating sound fields with an actively tunable metasurface, Proc. Natl. Acad. Sci. U. S. A. **115**, 6638 (2018).
[11] S. Rotter and S. Gigan, Light fields in complex media: mesoscopic scattering meets wave control, Rev. Mod. Phys. **89**, 015005 (2017).
[12] H. Cao, A. P. Mosk, and S. Rotter, Shaping the propagation of light in complex media, Nat. Phys. **18**, 994 (2022).
[13] J. Bertolotti and O. Katz, Imaging in complex media, Nat. Phys. **18**, 1008 (2022).
[14] P. Ambichl, A. Brandstötter, J. Böhm, M. Kühmayer, U. Kuhl, and S. Rotter, Focusing Inside Disordered Media with the Generalized Wigner-Smith Operator, Phys. Rev. Lett. **119**, 033903 (2017).
[15] P. del Hougne, R. Sobry, O. Legrand, F. Mortessagne, U. Kuhl, and M. Davy, Experimental realization of optimal energy storage in resonators embedded in scattering media, Laser Photonics Rev. **15**, 2000335 (2021).
[16] N. Bender, A. Yamilov, A. Goetschy, H. Yılmaz, C. W. Hsu, and H. Cao, Depth-targeted energy delivery deep inside scattering media, Nat. Phys. **18**, 309 (2022).
[17] J. Cao, Q. Yang, Y. Miao, Y. Li, S. Qiu, Z. Zhu, P. Wang, and Z. Chen, Enhance the delivery of light energy ultra-deep into turbid medium by controlling multiple scattering photons to travel in open channels, Light: Sci. Appl. **11**, 108 (2022).
[18] G. Montaldo, G. Lerosey, A. Derode, A. Tourin, J. de Rosny, and M. Fink, Telecommunication in a disordered environment with iterative time reversal, Waves Random Media **14**, 287 (2004).
[19] H. Zhao, Y. Shuang, M. Wei, T. J. Cui, P. del Hougne, and L. Li, Metasurface-assisted massive backscatter wireless communication with commodity Wi-Fi signals, Nat. Commun. **11**, 3926 (2020).
[20] M. F. Imani, S. Abadal, and P. del Hougne, Metasurface-programmable wireless network-on-chip, Adv. Sci. **9**, 2201458 (2022).
[21] X. Meng, R. Liu, H. Chu, R. Peng, M. Wang, Y. Hao, and Y. Lai, Through-Wall Wireless Communication Enabled by a Metalens, Phys. Rev. Appl. **17**, 064027 (2022).
[22] J.-F. Aubry, M. Tanter, J. Gerber, J.-L. Thomas, and M. Fink, Optimal focusing by spatio-temporal inverse filter. II. Experiments. Application to focusing through absorbing and reverberating media, J. Acoust. Soc. Am. **110**, 48 (2001).
[23] G. Montaldo, M. Tanter, and M. Fink, Real time inverse filter focusing through iterative time reversal, J. Acoust. Soc. Am. **115**, 768 (2004).
[24] J. Bercoff, M. Tanter, and M. Fink, Supersonic shear imaging: a new technique for soft tissue elasticity mapping, IEEE Trans. Ultrason. Ferroelectr. Freq. Control **51**, 396 (2004).
[25] W. Lambert, L. A. Cobus, M. Couade, M. Fink, and A. Aubry, Reflection Matrix Approach for Quantitative Imaging of Scattering Media, Phys. Rev. X **10**, 021048 (2020).
[26] Q. Wang, P. del Hougne, and G. Ma, Controlling the Spatiotemporal Response of Transient Reverberating Sound, Phys. Rev. Appl. **17**, 044007 (2022).
[27] M. del Hougne, S. Gigan, and P. del Hougne, Deeply Subwavelength Localization with Reverberation-Coded Aperture, Phys. Rev. Lett. **127**, 043903 (2021).
[28] P. del Hougne and G. Lerosey, Leveraging Chaos for Wave-Based Analog Computation: Demonstration with Indoor Wireless Communication Signals, Phys. Rev. X **8**, 041037 (2018).
[29] M. Rafayelyan, J. Dong, Y. Tan, F. Krzakala, and S. Gigan, Large-Scale Optical Reservoir Computing for Spatiotemporal Chaotic Systems Prediction, Phys. Rev. X **10**, 041037 (2020).
[30] J. W. Goodman, *Introduction to Fourier Optics*, 4th ed. (W. H. Freeman, New York, 2017).
[31] D. P. Kelly, Numerical calculation of the Fresnel transform, J. Opt. Soc. Am. A **31**, 755 (2014).
[32] F. Jacobsen and P. M. Juhl, *Fundamentals of General Linear Acoustics* (Wiley, West Sussex, 2013).
[33] I. M. Vellekoop, A. Lagendijk, and A. P. Mosk, Exploiting disorder for perfect focusing, Nat. Photonics **4**, 320 (2010).
[34] S. M. Popoff, G. Lerosey, M. Fink, A. C. Boccara, and S. Gigan, Controlling light through optical disordered media: transmission matrix approach, New J. Phys. **13**, 123021 (2011).
[35] A. Goetschy and A. D. Stone, Filtering Random Matrices: The Effect of Incomplete Channel Control in Multiple Scattering, Phys. Rev. Lett. **111**, 063901 (2013).
[36] B. Gerardin, J. Laurent, P. Ambichl, C. Prada, S. Rotter, and A. Aubry, Particlelike wave packets in complex scattering systems, Phys Rev B **94**, 014209 (2016).
[37] A. Aubry and A. Derode, Random Matrix Theory Applied to Acoustic Backscattering and Imaging In Complex Media, Phys. Rev. Lett. **102**, 084301 (2009).
[38] M. Tanter, J.-F. Aubry, J. Gerber, J.-L. Thomas, and M. Fink, Optimal focusing by spatio-temporal inverse filter. I. basic principles, J. Acoust. Soc. Am. **110**, 37 (2001).
[39] T. L. Szabo, *Diagnostic Ultrasound Imaging: Inside Out*, 2nd ed. (Academic press, Boston, 2014).
[40] J. Durnin, J. J. Miceli, and J. H. Eberly, Diffraction-Free Beams, Phys. Rev. Lett. **58**, 1499 (1987).
[41] D. Di Battista, D. Ancora, M. Leonetti, and G. Zacharakis, Tailoring non-diffractive beams from amorphous light speckles, Appl. Phys. Lett. **109**, 121110 (2016).
[42] G. A. Siviloglou, J. Broky, A. Dogariu, and D. N. Christodoulides, Observation of Accelerating Airy Beams, Phys. Rev. Lett. **99**, 213901 (2007).
[43] D. G. Papazoglou, N. K. Efremidis, D. N. Christodoulides, and S. Tzortzakis, Observation of abruptly autofocusing waves, Opt. Lett. **36**, 1842 (2011).
[44] Z. Pi, Y. Hu, Z. Chen, and J. Xu, Large-scale sharply bending paraxial beams, APL Photonics **4**, 056101 (2019).
[45] C. Draeger and M. Fink, One-Channel Time Reversal of Elastic Waves in a Chaotic 2D-Silicon Cavity, Phys. Rev. Lett. **79**, 407 (1997).
[46] F. Lemoult, G. Lerosey, J. de Rosny, and M. Fink, Manipulating Spatiotemporal Degrees of Freedom of Waves in Random Media, Phys. Rev. Lett. **103**, 173902 (2009).

[47] F. Lemoult, M. Fink, and G. Lerosey, Acoustic Resonators for Far-Field Control of Sound on a Subwavelength Scale, Phys. Rev. Lett. **107**, 064301 (2011).

[48] D. Andreoli, G. Volpe, S. Popoff, O. Katz, S. Grésillon, and S. Gigan, Deterministic control of broadband light through a multiply scattering medium via the multispectral transmission matrix, Sci. Rep. **5**, 10347 (2015).

[49] S. Tripathi, R. Paxman, T. Bifano, and K. C. Toussaint, Vector transmission matrix for the polarization behavior of light propagation in highly scattering media, Opt. Express **20**, 16067 (2012).

[50] Y. Guan, O. Katz, E. Small, J. Zhou, and Y. Silberberg, Polarization control of multiply scattered light through random media by wavefront shaping, Opt. Lett. **37**, 4663 (2012).